Energy & Environmental Science

ROYAL SOCIETY OF CHEMISTRY

PAPER

View Article Online
View Journal | View Issue

Cite this: *Energy Environ. Sci.*, 2025, **18**, 8475

Boosting the irregular wave energy harvesting performance of oscillating float-type TENGs *via* staggered alignment pairing-induced current superposition

Xianggang Dai,[abc] Long Qi,[abc] Shiyuan Chang,[abc] Qinghe Wu,[abc] Xiaobo Wu,[abc] Zhanyong Hong,*[abc] Tao Jiang *[abc] and Zhong Lin Wang*[ac]

Triboelectric nanogenerators (TENGs) show immense potential for harvesting low-frequency, chaotic, high-entropy ocean wave energy, offering a reliable power source for low-power sensors distributed across marine environments. However, their development remains constrained by limited power output and friction-related wear challenges. Here, we introduce an oscillating float-type triboelectric nanogenerator (OF-TENG) that boosts output current *via* staggered alignment pairing (SAP) of triboelectric materials, coupled with a planetary gear and non-contact reciprocating rotary design, to effectively capture multidirectional low-frequency ocean wave energy. At 1 Hz low-frequency waves, the OF-TENG delivers an output current of 0.31 mA, a peak power of 111.56 mW, and an average volumetric power density of 21.58 W m^{-3}. Leveraging its non-contact friction design, the OF-TENG sustains exceptional output stability after 60 hours (>9 500 000 cycles) of continuous operation, with no significant performance decline. Additionally, the OF-TENG successfully powers 1000 light emitting diodes, a wireless water quality monitoring system (measuring total dissolved solids, pH value, and temperature), and drives electrochemical water splitting, yielding a hydrogen generation rate of 16.04 μL min^{-1} after 30 min. This study propels the development of high-power-density OF-TENGs, underscoring their substantial potential for harvesting low-frequency and chaotic wave energy and energizing distributed sensors in marine Internet of Things applications.

Received 8th May 2025,
Accepted 25th July 2025

DOI: 10.1039/d5ee02523k

rsc.li/ees

Broader context

Ocean waves contain vast low-frequency and chaotic energy, which can deliver reliable power to distributed sensors in marine Internet of Things systems when harnessed as a clean, renewable, and sustainable resource. Triboelectric nanogenerators (TENGs) exhibit high power density, efficiency, lightweight design, and low fabrication costs, with the power density scaling linearly with a frequency below 5 Hz. Yet, their progress remains hindered by challenges including limited power output, wave direction dependency, and frictional wear. Here, we introduce an oscillating float-type TENG (OF-TENG) that overcomes these constraints using staggered alignment pairing (SAP) of triboelectric materials and a non-contact reciprocating rotary design with planetary gears, enabling efficient multidirectional wave energy harvesting. At 1 Hz, it delivers an output current of 0.31 mA, a peak power of 111.56 mW, and an average volumetric power density of 21.58 W m^{-3}, maintaining performance stability after 60 hours (>9 500 000 cycles). In real-world water wave testing, it effectively powers low-energy water quality sensors and electrochemical water splitting. This study offers critical new strategies for designing advanced energy harvesting devices, with applications in large-scale blue energy harvesting and intelligent marine monitoring.

1. Introduction

The emergence of ocean monitoring in the Internet of Things (IoT) era hinges on delivering stable energy supplies to extensive distributed sensor networks.[1] Low-frequency, chaotic, high-entropy ocean wave energy represents a vast yet underutilized renewable resource, spanning over 70% of the Earth's surface.[2–4] Conventional electromagnetic generators (EMGs)

[a] *Beijing Key Laboratory of High-Entropy Energy Materials and Devices, Beijing Institute of Nanoenergy and Nanosystems, Chinese Academy of Sciences, Beijing 101400, P. R. China. E-mail: jiangtao@binn.cas.cn, hongzhanyong@binn.cas.cn, zhong.wang@mse.gatech.edu*
[b] *School of Nanoscience and Engineering, University of Chinese Academy of Sciences, Beijing 100049, P. R. China*
[c] *Guangzhou Institute of Blue Energy, Knowledge City, Huangpu District, Guangzhou 510555, P. R. China*

struggle to capture this high-entropy energy, due to their inefficiency at low frequencies (<5 Hz), compounded by their large size and high cost.[5–7] Driven by Maxwell's equations and based on triboelectrification and electrostatic induction,[8–12] triboelectric nanogenerators (TENGs) offer a lightweight,[13,14] cost-effective solution,[15,16] converting low-frequency,[17–19] random-amplitude wave motion into electricity to power distributed marine sensor networks.[20,21] Yang *et al.*[22] developed a TENG based on an oscillating water column (OWC) system, employing an air turbine mechanism to transform wave-induced fluid oscillations into rotational energy to produce triboelectric outputs. Zhang *et al.*'s pendulum structure accommodates multi-directional motion,[23] yet its energy conversion efficiency is constrained under low wave height and low-frequency conditions. Gonçalves *et al.*[24] identified that the relative speed of the contact-separation process in rolling ball structures critically influences output power, though sustaining continuous contact under irregular waves poses a challenge. The solid–liquid contact triboelectric system by Li *et al.*[25] shares a similar working principle with the OF-TENG in this study, yet its output relies on specific vortex excitation paths, restricting its versatility and deployment flexibility. Beyond their role in harvesting low-frequency ocean wave energy, TENGs are increasingly applied in biomedical fields, powering *in vivo* and wearable systems, which highlights their interdisciplinary potential in healthcare.[26,27] Considering that output energy is proportional to the square of current, optimizing TENG device structures to achieve stable, higher-output currents remains a critical challenge.

Over years of exploration, researchers have developed various novel TENG energy harvesting devices to enhance output performance, focusing on structural optimization, including bioinspired designs,[28–30] spring oscillator structures,[31–34] and rotary structures.[35–38] Among these, rotary structures convert low-frequency ocean wave motion into high-frequency mechanical motion, achieving optimal energy conversion efficiency.[22] Moreover, rotary structures typically utilize sliding contact, flexible friction, and non-contact friction strategies to minimize mechanical wear and prolong operational lifespan, yet their electrical output performance remains relatively limited.[39,40] Nevertheless, the instability of charge density at the frictional interface, coupled with losses from air breakdown, limits the performance gains achievable with these approaches. Furthermore, under authentic oceanic wave conditions, vertical wave energy, owing to its greater amplitude and energy density, holds substantial potential, yet it has largely been neglected in prior TENG architectures.[41] Additionally, the stochastic and multidirectional nature of low-frequency oceanic waves presents further challenges to conventional pendulum-based TENG energy harvesters, which are generally tailored to unidirectional wave scenarios.[42–44] Consequently, there is a pressing demand for a TENG that combines output enhancement strategies with novel energy conversion mechanisms to effectively harvest multidirectional, low-frequency vertical wave energy and transform it into high-frequency energy, substantially boosting overall energy harvesting efficiency.

In this work, we introduce an oscillating float-type triboelectric nanogenerator (OF-TENG) that integrates staggered alignment pairing (SAP) of triboelectric materials to boost output current, and a non-contact reciprocating rotary design, for capturing and converting multidirectional wave energy. This design achieves SAP by introducing triboelectric material pairs with different electronegativities into the rotor and stator, enabling the superposition of output currents from both components. In the structural design, we adopt a spiral structure, rigidly connecting the spiral tube to a planetary reducer, and rigidly coupling the planetary reducer's rotation shaft to the rotor. Accelerated by the planetary reducer, this configuration transforms vertical wave oscillations into reciprocating rotation of the spiral tube through a spiral ring, driving the rotor into high-frequency reciprocation, even under low-frequency wave conditions. At a low frequency of 1 Hz, the OF-TENG delivers an output current of about 0.31 mA, a peak power of 111.56 mW, and an average volumetric power density of 21.58 W m^{-3}. Owing to the non-contact friction between the rotor and stator, the OF-TENG sustains exceptional output stability after 60 h of continuous operation (>9 500 000 cycles), with no significant performance degradation. Finally, we demonstrate the high-output applications of the OF-TENG: directly powering 1000 light emitting diodes (LEDs), successfully driving a wireless water quality monitoring system (measuring total dissolved solids (TDS), pH value, and temperature), and producing hydrogen and oxygen in real time through water electrolysis. This indicates that the OF-TENG exhibits immense potential for large-scale blue energy harvesting and as a distributed power solution in marine IoT applications.

2. Results and discussion

2.1. Structural design and operation mechanism of the OF-TENG

Low-frequency, chaotic wave energy is ubiquitous in the ocean. To capture such energy, we propose a device employing the OF-TENG network to harvest and convert wave energy into electricity. Fig. 1(a) illustrates the application scenarios of the OF-TENG through harvesting ocean wave energy. Multiple OF-TENG units can be networked and deployed near islands or buoys to power sensors, wireless monitoring systems, and water quality devices. In addition, this device can also provide energy for water splitting systems, promoting the development of self-powered devices and the blue economy, with significant application potential. Fig. 1(b) presents a schematic diagram of a single OF-TENG floating on the water surface in marine environments. The device is encased in a spherical acrylic shell to improve buoyancy and structural stability, ensuring reliable performance across diverse sea conditions. The top floating unit is rigidly linked to a seabed-anchored point *via* a stainless steel optical axis, securing the device against displacement or drift induced by wave dynamics. To reduce friction resistance during the operation of the floating device, a linear sliding bearing is installed between the floating unit and the stainless steel optical axis, facilitating smooth wave-driven motion while

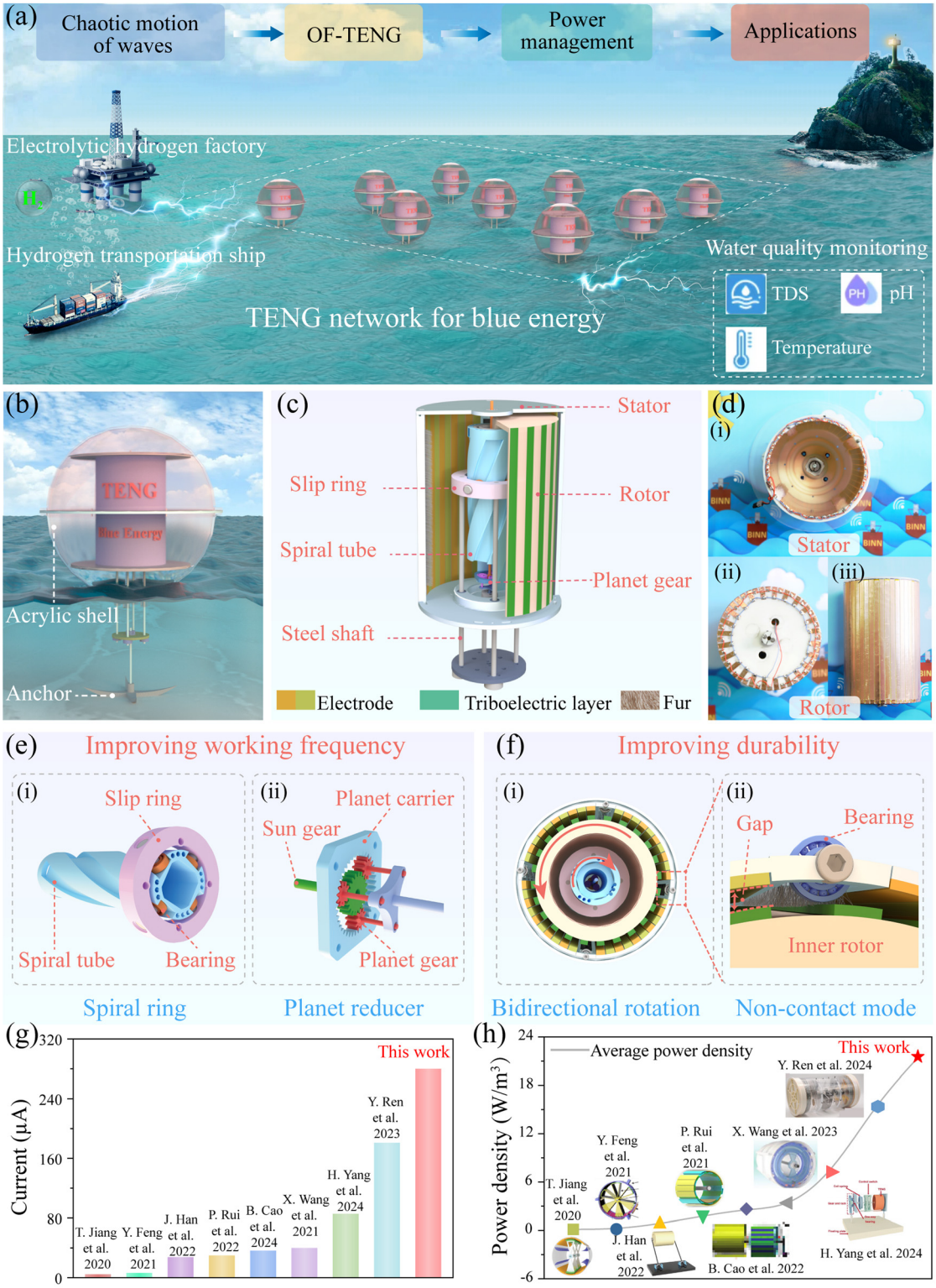

Fig. 1 Application background, structural design and operation mechanism of the OF-TENG. (a) Schematic diagram of the application scenarios for the OF-TENG, utilized for harvesting ocean blue energy to supply power for water quality monitoring and water electrolysis. (b) Sketch of the OF-TENG in a floating state in the ocean. (c) 3D cross-sectional view illustrating the overall structure of the OF-TENG. (d) Optical images of the stator (i) and rotor (ii, iii). (e) Structural schematics of the spiral ring (i) and planetary gear reducer (ii). (f) Top-view schematic of the OF-TENG (i), with an enlarged view of non-contact friction between the rotor and stator (ii). Output current (g) and average output power density (h) of the OF-TENG in comparison with other TENGs.

mitigating mechanical wear and structural fatigue. The design of the floating unit centers on leveraging the vertical oscillatory behavior of ocean waves, harnessing wave energy efficiently *via* the periodic motion of the structure and converting it into usable electrical power.

The 3D internal structure of the OF-TENG is shown in Fig. 1(c), comprising a stator cylinder, rotor cylinder, slip ring, spiral tube, planetary reducer, and four stainless steel shafts. Within this system, the planetary reducer's bottom rotating shaft is anchored to the stator cylinder, preventing free rotation induced by external motion. The spiral tube is embedded within the planetary reducer shell, with the rotating steel shaft at the top of the reducer passing through its center, and is rigidly coupled to the upper rotor cylinder *via* a limiter. Moreover, four stainless steel shafts are linked to the spiral ring through linear bearings installed at the base of the stator cylinder. When external waves act on the floating device, the stainless steel shafts undergo vertical motion, synchronously rotating the attached spiral ring and subsequently driving the spiral tube. This rotational motion engages the planetary reducer, inducing counter-rotation of the rotor cylinder (energy conversion animation as shown in Movie S1). Photographs of the stator cylinder and rotor cylinder are shown in Fig. 1(d)-(i)–(iii).

The system comprises two critical components: one designed to enhance operating frequency (Fig. 1(e)-(i), (ii)) and the other to improve durability and output current (Fig. 1(f)-(i), (ii)). Under wave excitation, the spiral ring (Fig. 1(e)-(i)) drives the rotor cylinder to perform reciprocating rotation. Facilitated by the planetary reducer (Fig. 1(e)-(ii)), this rotational motion effectively elevates the TENG's operating frequency, substantially improving wave energy conversion efficiency. Moreover, the stator and rotor cylinders feature the SAP of triboelectric materials (Nylon/Cu, polytetrafluoroethylene (PTFE)/Cu), enabling a current superposition effect that yields a total output of "1 + 1 = 2" (Fig. 1(f)-(i)). Concurrently, rolling bearings mounted on the stator cylinder ensure stable rotor cylinder motion and maintain an optimal gap (approximately 1 mm) between the friction layers of the stator and rotor cylinders (Fig. 1(f)-(ii)), enhancing system stability and longevity. Additionally, based on the triboelectric series and prior studies, materials with higher electronegativity acquire electrons more readily during triboelectrification, facilitating charge transfer within the device.[1,15] Rabbit fur exhibits significantly lower electronegativity than PTFE, making it an ideal positively charged material, whereas PTFE carries high-density negative charges, and nylon serves as a moderately polar material. This configuration optimizes charge distribution and coupling. Consequently, in the OF-TENG (using untreated and unmodified rabbit fur, nylon, and PTFE), rabbit fur, exhibiting high electropositivity and low friction resistance, is chosen as the triboelectric excitation material, fixed within the stator cylinder's groove, and supplementing charges to the PTFE surface during rotor rotation. Moreover, the inherent flexibility of rabbit fur minimizes wear on the PTFE film on the inner rotor surface during non-contact relative rotation of the inner and outer rotors in the OF-TENG, thereby preserving high output performance. Additionally, the core device is encased in a corrosion-resistant polymer shell, ensuring exceptional mechanical stability.

Owing to its capability for current superposition, high stability, and enhanced durability, the OF-TENG exhibits markedly superior output performance compared to previously reported non-contact TENGs. Experimental results reveal that the OF-TENG achieves an output current of 0.31 mA (Fig. 1(g)) and a volumetric average power density of 21.58 W m^{-3} (Fig. 1(h)), demonstrating excellent capability in harvesting and converting ocean wave energy.

2.2. Optimization for the SAP of triboelectric materials in the OF-TENG

In conventional freestanding sliding TENGs, the rotor cylinder's friction layer typically features a periodic PTFE-blank-PTFE arrangement, with the stator cylinder primarily composed of copper electrodes. However, the blank friction areas in this design do not contribute effectively to triboelectrification, thereby constraining the TENG's output performance. In this study, an innovative SAP design of electrodes and friction layers is introduced to fully leverage the blank friction areas on the rotor cylinder. Specifically, copper electrodes are affixed to the bases of the rotor and stator cylinders, with PTFE and Nylon layers adhered on their surfaces, creating an SAP of Cu/PTFE-Cu/Nylon (stator) and Cu/Nylon-Cu/PTFE (rotor). This facilitates effective superposition of the output currents from the stator and rotor, as depicted in the cross-sectional schematic of the basic circuit connection in Fig. 2(a).

Additionally, rabbit fur is incorporated on the stator cylinder as a charge-replenishing material to enhance the surface charge density of the friction layer. Rabbit fur, characterized by its high hair density and nanoscale fiber diameter, significantly increases the contact area of the friction layer, ensuring intimate contact with minimal friction resistance, thereby enabling the PTFE film to gain more triboelectric charges. Fig. 2(b) uses a quarter cross-section of the cylindrical electrode to elaborate on the working principle of the OF-TENG. Based on the charge affinity and triboelectric series of the materials, the order is PTFE > rabbit fur > Nylon. The staggered electrode connections on the stator and rotor result in the formation of two pairs of parallel electrodes on each during operation of the power generation unit. In parallel connection mode (Fig. 2(b)-(i)), the rotor's Cu/PTFE and Cu/Nylon are paired with the stator's Cu/Nylon and Cu/PTFE, respectively, forming SAP of triboelectric materials. Upon external excitation, clockwise rotation of the rotor cylinder (Fig. 2(b)-(ii)) induces a charge mismatch between the Cu electrodes on the rotor and stator, generating a potential difference that drives free electrons to flow through the load, producing current. Continued rotation of the rotor cylinder (Fig. 2(b)-(iii)) reverses the current direction, yielding opposing current signals (Fig. 2(b)-(iv)). Since both the stator and rotor cylinder exhibit induced potential differences, the total output current is the superposition of the two, effectively enhancing the output performance of the TENG.

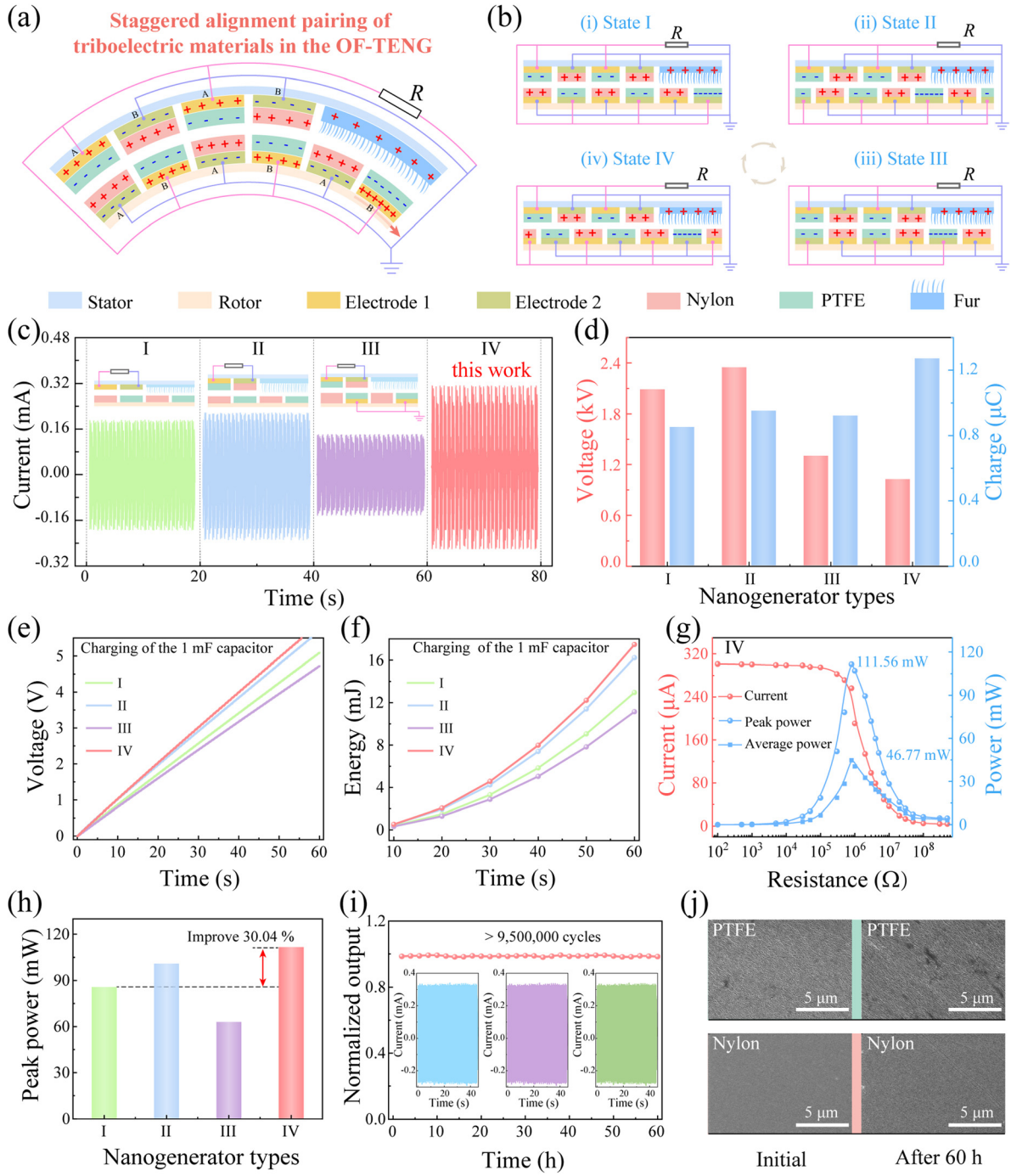

Fig. 2 (a) Schematic illustrating the principle of SAP of triboelectric materials and electrode connections in the OF-TENG, (b) current superposition mechanism during periodic sliding cycles. (c) Dynamic output current curves of the OF-TENG for different SAP methods of triboelectric materials, (d) corresponding variations in output voltage and transferred charge, (e) charging process of a 1 mF capacitor, (f) calculation of the energy stored in the 1 mF capacitor. (g) Output current, peak power, and average power of the OF-TENG *versus* load resistance for the SAP method IV of triboelectric materials. (h) Comparison of peak output power of the OF-TENG for four distinct SAP methods of triboelectric materials. (i) Durability performance of the OF-TENG under the SAP method IV of triboelectric materials after the test of 60 h. (j) SEM images of the friction layers (PTFE, Nylon) on the rotor cylinder before the tests and after the tests of 60 h. All experiments were performed at a frequency of 1 Hz and an amplitude of 15 cm.

To thoroughly assess the output performance of the OF-TENGs with different triboelectric material pairing methods, we systematically examined the impacts of four pairing approaches on the output characteristics at a linear motor frequency of 1 Hz and an amplitude of 15 cm (Fig. 2(c)). Initially, with the stator featuring only Cu electrodes and the rotor composed of periodic Nylon-PTFE friction layers, the OF-TENG yields an output current of ~0.18 mA (Fig. 2(c)-(I) and Fig. S1(I)), an output voltage of ~2.0 kV, and transferred charges of 0.85 μC (Fig. 2(d)-(I) and Fig. S2(a), (b)). Then,

incorporating periodic PTFE-Nylon friction layers onto the stator electrodes enhances the electrostatic induction effect, boosting effective charge transfer between friction layers and elevating the output current to 0.21 mA (Fig. 2(c)-(II) and Fig. S1(II)). Furthermore, attaching a grounded Cu electrode beneath the rotor's PTFE friction layer reduces the OF-TENG's output current to 0.14 mA (Fig. 2(c)-(III) and Fig. S1(III)), with concurrent reductions in output voltage and transferred charge (Fig. 2(d)-(III)), which is attributed to the grounded electrode altering the electric field distribution and dissipating a portion of charges *via* the grounding pathway.

Lastly, when Cu/PTFE and Cu/Nylon are affixed to the stator and rotor surfaces, respectively, to form the SAP of triboelectric materials, the system's output characteristics display marked variations. According to the equivalent circuit model of a TENG, each unit is represented as a voltage source in series with a variable capacitor, functioning as an independent triboelectric charge-generating entity. When connected in parallel, friction units on the stator and rotor both generate charges that accumulate, with charge transfer producing a current, elevating the total output current to 0.31 mA (Fig. 2(c)-(IV)). However, the parallel configuration increases the system's equivalent capacitance, so that, based on the $V = Q/C$ relationship, the augmented capacitance counteracts the increased charge, lowering the total output voltage (Fig. 2(d)-(IV)).

As depicted in Fig. 2(e), we further investigated the effects of four distinct pairing configurations on the charging rate of the OF-TENG to a 1 mF capacitor. The results demonstrate that with the SAP of triboelectric materials formed on the stator and rotor, the OF-TENG attains the highest charging rate, maximizing energy storage in the capacitor within the same duration (Fig. 2(f)). Furthermore, the output current, peak power, and average power of the OF-TENG vary with load resistance, as depicted in Fig. 2(g). At 800 kΩ, the OF-TENG achieves a peak

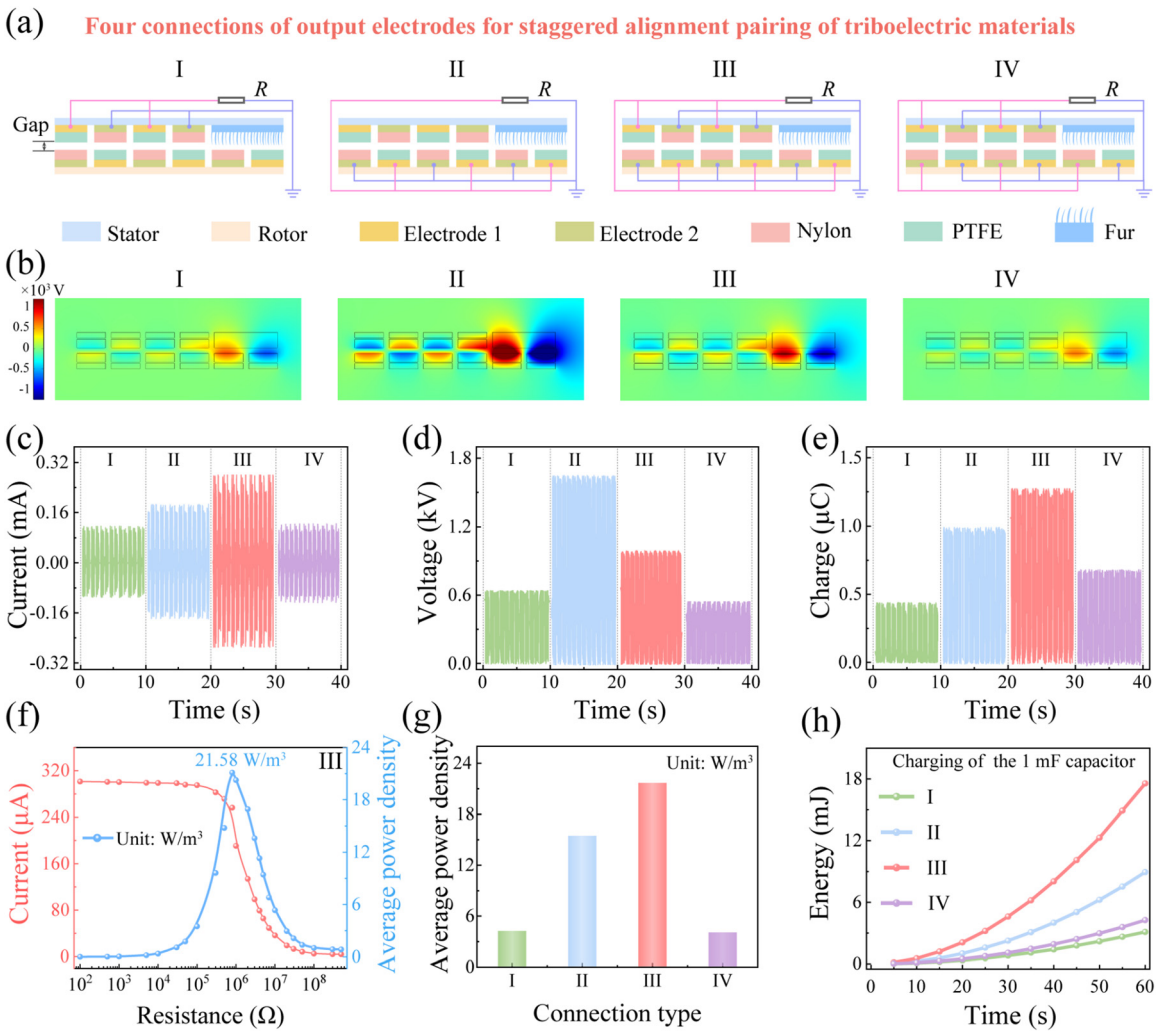

Fig. 3 Operational principles and electrical performance of the OF-TENG with staggered friction layer pairing under various output electrode configurations. (a) Schematics illustrating the four connection configurations (I–IV). (b) Simulated electric field distributions for configurations I–IV of output electrode connections. (c) Output current, (d) output voltage, and (e) transferred charge for different configurations. (f) In configuration III, the output current and average power density of the OF-TENG are shown at different load resistances. (g) Comparison of the average power densities of the OF-TENGs under four configurations. (h) Stored energy curves of a 1 mF capacitor under different configurations.

power of 111.56 mW and an average power of 46.77 mW, representing an increase of ~30.04% in peak and average power compared to configuration I. (Fig. S3(a)–(c)). Additionally, the OF-TENG exhibits exceptional stability, showing no notable decline in output performance after 60 hours (>9 500 000 cycles) of continuous cycling (Fig. 2(i)). Concurrently, SEM analysis of PTFE and Nylon film surfaces shows no discernible damage or scratches after 60 hours of non-contact triboelectric operation, reinforcing the durability of the device design (Fig. 2(j)).

2.3. Connection configurations of output electrodes under SAP of triboelectric materials in the OF-TENG

In the proposed OF-TENG, where the triboelectric materials of the stator and rotor adopt an SAP strategy, the effects of different connection configurations (I–IV) of output electrodes (electrode 1 and electrode 2) on the electrical performance were systematically analyzed. As illustrated in Fig. 3(a), the four configurations are I (stator electrode), II (rotor electrode), III (stator and rotor electrodes in parallel), and IV (stator and rotor electrodes in series). Using COMSOL Multiphasic electrostatic and circuit modules, we simulated the electric field distributions arising from interactions across the four connection configurations (Fig. 3(b)-(I)–(IV)), demonstrating that the electrode connectivity influences local field distributions, consequently affecting charge transfer efficiency and output performance. Experimental data (Fig. 3(c)–(e)) reveal maximum peak currents of 0.13, 0.18, 0.3, and 0.12 mA, peak voltages of 0.64, 1.64, 1.02, and 0.54 kV, and transferred charges of 0.44, 0.98, 1.35, and 0.68 μC for the four configurations, respectively. Relative to the I configuration, the II one shows enhanced current, voltage, and charge, attributed to friction-induced excitation and charge replenishment by rabbit fur on the stator during rotor rotation. The parallel configuration of III follows circuit physics, with superimposed currents and charges from stator and rotor electrodes markedly boosting output current and transferred charge, though the output voltage reflects an average of individual electrode voltages. In the series configuration of IV, constrained by the TENG's internal impedance, the voltage decreases nonlinearly, whereas the current and charge remain relatively stable. Further examination of power output characteristics (Fig. 3(f)) reveals that, at an 800 kΩ load, the III configuration attains an average volumetric power density of 21.58 W m^{-3}, which is 4.97, 1.40, and 5.42 times greater than the I (4.34 W m^{-3}), II (15.36 W m^{-3}), and IV (3.98 W m^{-3}) ones, respectively (Fig. 3(g) and Fig. S4a–c). Concurrently, among the four connection configurations, the III one demonstrates the highest energy storage rate for a 1 mF capacitor, reinforcing its superiority for energy harvesting applications (Fig. 3(h) and Fig. S5a–d).

2.4. Performance of the OF-TENG in water wave environments

The wave energy harvesting capability of the OF-TENG was demonstrated in an artificial wave pool (45 m in length, 4 m in width, and 3 m in depth). As shown in Fig. 4(a), the OF-TENG device is fixed to the bottom of the wave pool *via* anchor points, and its motion states at different stages of the wave cycle (crest, middle, and trough) are demonstrated. The OF-TENG, anchored to the seabed, is designed to withstand position variations from continuous sea surface motion. Its robust anchoring system and flexible tether minimize mechanical stress, ensuring stability. Subsequently, the output performance of the OF-TENG was systematically evaluated at wave heights of 6–15 cm and frequencies of 0.4–1.2 Hz. The results demonstrate that, at a fixed wave height of 15 cm, the output current increases significantly with the frequency and stabilizes beyond 1.0 Hz, reaching a maximum of approximately 0.30 mA at 1.0 Hz (Fig. 4(b)). The output voltage (Fig. S6a) and transferred charge (Fig. S6b) remain independent of the frequency. Similarly, at a fixed frequency of 1.0 Hz, the output current increases with the wave height, while the output voltage (Fig. S7a) and transferred charge (Fig. S7b) are wave height-independent. Due to the inherent structural characteristics of the OF-TENG, its maximum up-down fluctuation displacement is 15 cm. Under lower-frequency and lower-amplitude conditions (*e.g.*, 0.2–0.5 Hz, 5–10 cm), the OF-TENG remains operational, despite slightly reduced electrical outputs. Furthermore, the OF-TENG can stably harvest wave energy across an angle range from 0° to 360°, with its output performance nearly unaffected by the change in wave direction (Fig. 4(d)). Considering the dynamic characteristics of ocean waves, we performed a 24-hour output performance test on the OF-TENG under sinusoidal wave excitation in a wave pool (see Fig. S8 and S9). The results indicate that the output performance remains stable across the entire test duration, with no notable degradation detected. The inset further presents output current profiles for the initial, intermediate, and final stages, confirming the device's robust long-term operational stability. The single current output characteristics of the OF-TENG are presented in Fig. 4(e). To more accurately simulate the real ocean environment, we implemented Pierson–Moskowitz (P–M) irregular waves and performed a performance evaluation of the OF-TENG in the wave pool (Fig. S10). As depicted in Fig. 4(f) and Fig. S11a, b, the device exhibits stable outputs under multi-frequency and multi-amplitude wave excitations, highlighting its robust environmental adaptability. The OF-TENG transforms mechanical energy into electrical energy, regulated *via* a power management circuit (PMC), to power end devices (Fig. 4(g)). Effective power management is enabled when the voltage across C1 surpasses the breakdown voltage of the silicon control rectifier (SCR). This power management circuit is universally compatible with all modes of TENGs.[45] Voltage curves for the OF-TENG charge a 1 mF capacitor through the PMC for various frequencies (Fig. 4(h)) were measured, confirming its effective operation under low-frequency, chaotic wave conditions. Moreover, with the PMC, the OF-TENG charges a 1 mF commercial capacitor from 0 V to 16.5 V in 60 s, compared to just 5.2 V without PMC over the same duration, exhibiting a ~10-fold increase in charging efficiency (Fig. 4(i) and Fig. S12).

2.5. Application demonstration of the OF-TENG

The OF-TENG can harvest ocean wave energy and transform it into electrical energy, delivering a sustainable power source for marine IoT systems, as depicted in Fig. 5(a). It can power LEDs, water quality monitoring, and electrochemical hydrogen production systems, demonstrating broad application potential.

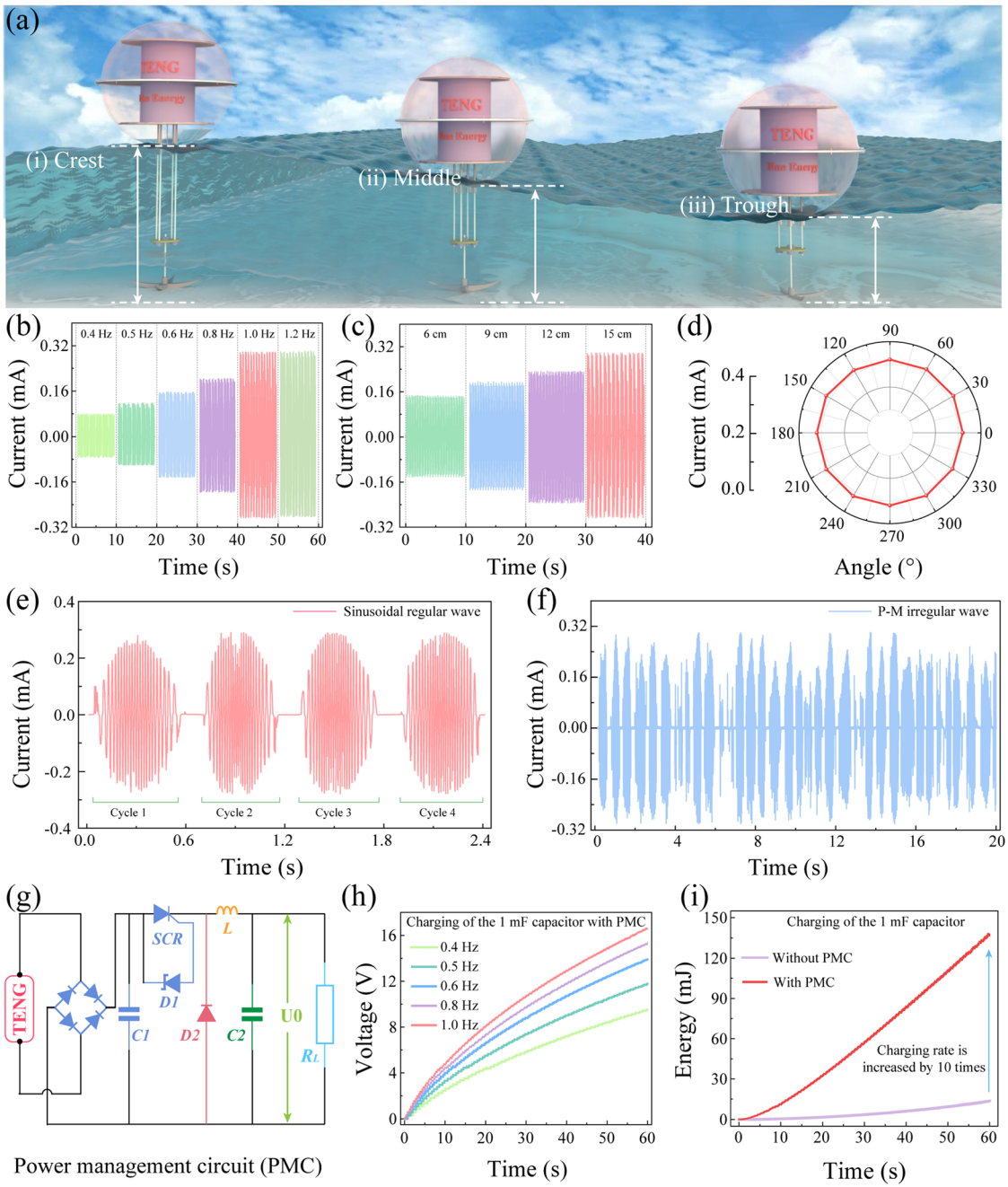

Fig. 4 Performance evaluation of the OF-TENG in real water wave environments. (a) Schematic illustrating the OF-TENG at various stages of water wave motion. Output current curves of the OF-TENG for (b) varying wave frequencies at a fixed wave height of 15 cm and (c) wave heights at a fixed frequency of 1 Hz. (d) Radar chart of the OF-TENG's current with response to excitation waves generated at an interval of 30° from 0° to 360°. Output current curves of the OF-TENG under (e) sinusoidal and (f) P–M irregular waves at the frequency of 1 Hz and the wave height of 15 cm. (g) Circuit diagram of the PMC connected to a backend load. (h) Voltage curves on a 1 mF capacitor charged by the OF-TENG with the PMC for varying frequencies. (i) Stored energy on the 1 mF capacitor charged by the OF-TENG with and without the PMC. All tests were conducted at a frequency of 1 Hz and a wave height of 15 cm.

Under water wave excitation, the OF-TENG simultaneously illuminates 1000 green LEDs (Fig. 5(b) and Movie S2), enabling its design as a digital panel for navigation signaling, such as buoy lights. Furthermore, the OF-TENG powers a water quality monitoring system (Fig. 5(c)), comprising the OF-TENG, PMC, LTC3588-1, and water quality sensors, enabling self-sustained environmental monitoring. With the PMC, the OF-TENG efficiently charges a 22 mF capacitor to 3.8 V in 56 s, subsequently powering the water quality monitoring system through the LTC3588-1 module. Thereafter, the voltage decreases to 3.2 V, initiating the next charging cycle. Over a charging interval of 12 s, the water quality monitoring system continuously monitors and transmits data about four solutions (deionized water, HCl, NaOH, and river water), as illustrated in Fig. 5(d) and Movie S3.

The OF-TENG's performance in powering water electrolysis for hydrogen generation was further explored. The electrolysis

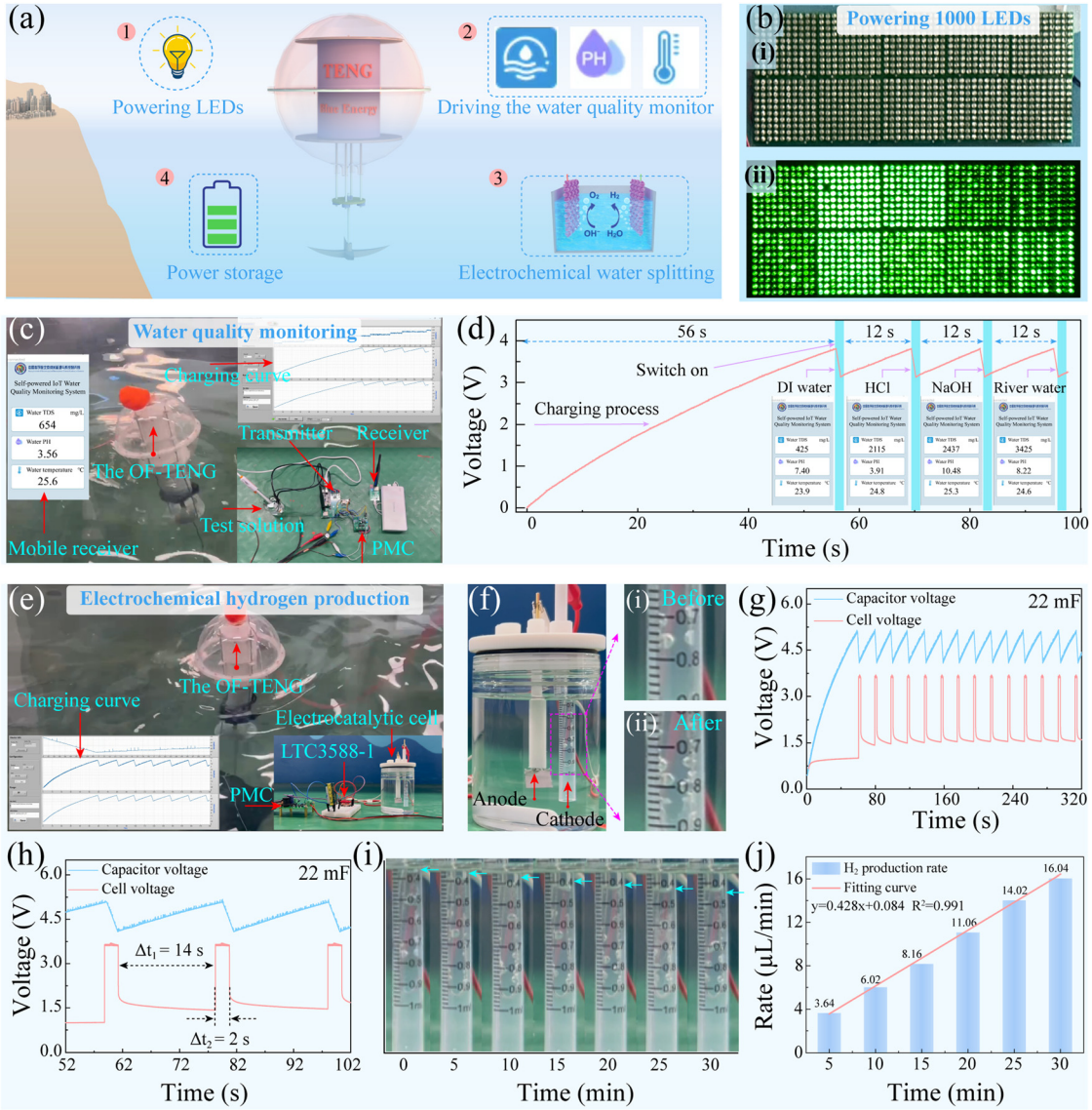

Fig. 5 Demonstration of OF-TENG applications. (a) Prospects for the maritime applications of the OF-TENG. (b) Photographs of the OF-TENG powering 1000 LEDs in real water before (i) and after (ii). (c) Diagram of the OF-TENG driving an electronic switch for water quality monitoring. (d) Voltage profile on a 22 mF commercial capacitor for four different solutions (deionized water, HCl, NaOH, river water) for water quality sensing and monitoring. The insets show the water quality data received from different solutions. (e) Diagram of an electrochemical water splitting system powered by the OF-TENG through charging the 22 mF capacitor *via* the LTC3588-1 module. (f) Photograph of the water electrolysis setup, with enlarged views (i) before and (ii) after hydrogen generation. (g) Time-dependent relationship between the 22 mF capacitor voltage and electrolysis cell voltage. (h) Enlarged plot of voltages on the LTC3588-1 module and electrolysis cell with respect to time. (i) Photographs of gases collected in a 1.0 M NaOH solution within the collection tube at various time stages. (j) H_2 generation rates with the time stages in a continuous test of 30 min. All tests were conducted in a wave pool at a wave height of 15 cm and a frequency of 1.0 Hz.

system comprises the OF-TENG, PMC, Pt electrodes, and 1.0 M NaOH solution, as depicted in Fig. 5(e). To assess the hydrogen ield of the OF-TENG electrolysis system, gas was collected using a hydrogen collection tube (Fig. 5(f)), showing no discernible bubbles initially (i) and dense H_2 bubbles after start (ii). In the electrolysis cell, the cathode and anode generate hydrogen and oxygen bubbles, respectively, *via* water electrolysis reactions (cathode: $2H_2O + 2e^- \rightarrow H_2 + 2OH^-$; anode: $2OH^- + 1/2e^- \rightarrow H_2O + 2e^-$), theoretically requiring 1.23 V,[46] though practical operation demands 1.5–2.0 V due to overpotential, bubble effects at the electrode surface, and system resistance losses. To provide adequate power, the OF-TENG charges a 22 mF capacitor through the PMC to 5.0 V, followed by discharge *via* the LTC3588-1 module, sustaining a steady output of 3.6 V in the electrolysis cell for 2 s (Fig. 5(g) and (h)). Stable bubble formation was observed on the Pt wire electrode during the experiment (Movie S4). When the cell voltage falls to 1.5 V, bubble production on the Pt wire electrode stops, which prompts the OF-TENG to recharge the 22 mF capacitor to 5.0 V over 14 s, repeating the discharge cycle thereafter. Concurrently, results from the hydrogen collection tube (Fig. 5(i)) indicate a gradual rise in H_2 yield over time, alongside a declining liquid level in the tube.

Furthermore, Fig. 5(j) illustrates the variation of H_2 generation rate with the time stages during 30 min of continuous OF-TENG operation, peaking at 16.04 μL min^{-1} after 30 min. In order to better evaluate the excellent performance of the hydrogen evolution rate in this work, as shown in Fig. S13 and Table S2, the hydrogen production rate is significantly improved compared with the published work. These applications underscore the OF-TENG's ability to efficiently harvest low-frequency wave energy for diverse energy needs, emphasizing its potential for large-scale wave energy harvesting. Future research will increasingly focus on addressing the complexities of deploying modular OF-TENG arrays, particularly in optimizing anchoring systems, scalable structural designs, and efficient electrical interconnections for practical marine energy harvesting.

3. Conclusions

In this work, we engineered an OF-TENG to harvest and convert vertical wave energy under low-frequency, chaotic, and multi-directional conditions. The OF-TENG incorporates the SAP of triboelectric materials with a non-contact reciprocating rotary design to efficiently capture multidirectional low-frequency ocean wave energy. The OF-TENG's output performance varies markedly with electrode configurations (I–IV), with configuration III (parallel stator–rotor electrodes), delivering a peak current of 0.31 mA, a peak power of 111.56 mW, and an average volumetric power density of 21.58 W m^{-3} at a load resistance of 800 kΩ. Non-contact friction imparts exceptional durability, showing no notable performance degradation or surface damage after 60 hours (>9 500 000 cycles). Under real water wave conditions at a wave height of 15 cm and a frequency of 1 Hz, the OF-TENG demonstrates robust adaptability, with output current increasing with wave height and frequency, and consistent energy harvesting across any wave direction. Practical demonstrations highlight the OF-TENG's potential, powering 1000 LEDs and water quality monitoring systems (*e.g.*, TDS, pH, and temperature) in different solutions. Additionally, it powers electrochemical water splitting, yielding a H_2 generation rate of 16.04 μL min^{-1} after 30 min. This study offers an efficient TENG design for large-scale ocean blue energy harvesting, underscoring its potential for future marine applications.

4. Experimental

4.1. Fabrication of the OF-TENG

The main components of the OF-TENG, including the stator cylinder, rotor cylinder, and helical ring, were all manufactured using 3D printing technology. The stator cylinder features four internal grooves designed to hold rabbit furs (purchased from Hengshui Yuyang Fur Co., Ltd) as charge supplementation materials. Copper foil electrodes, with a gap of 1 mm, are affixed to the inner wall of the stator cylinder. There are eight Cu electrodes in total, with one groove reserved for attaching rabbit fur *via* 3 M double-sided tape. PTFE (thickness: 80 μm) and Nylon (thickness: 25 μm) films are alternately layered onto the Cu electrodes, with two wires soldered to the Cu electrodes to connect the stator electrodes externally. The friction layers and electrodes of the rotor cylinder are crafted on a fiberglass board using a laser cutter (PLS 6.75), starting with evenly spaced cuts for the friction layers, followed by sequential attachment of Cu electrodes, overlaying alternating PTFE and Nylon films, and securing them to the rotor cylinder with 3 M adhesive. Subsequently, the bottom rotating shaft of the planetary reducer is fixed to the stator cylinder, the helical tube is tightly embedded in the planetary reducer housing, and the top rotating shaft passes through the helical tube, rigidly connected to the top rotor cylinder using a limiter. Furthermore, four stainless steel shafts, mounted to linear bearings at the stator cylinder base, are connected to the helical ring, allowing vertical axial sliding. The springs and bearings employed in the OF-TENG are industrial-grade standardized components, exhibiting validated fatigue life and mechanical stability. Ultimately, the assembly is encapsulated in an acrylic sphere coated with a multilayer corrosion-resistant system engineered to endure harsh marine environments and ensure long-term TENG stability. The base layer, Jotamastic 87, an epoxy coating renowned for its robust corrosion resistance, is complemented by a subsequent PPG Amercoat layer offering UV protection and enhanced durability.

4.2. Output measurement and material characterization of the OF-TENG

Output current and transferred charge were measured with a Keithley 6514 electrometer, while the output voltage was assessed using an HVP-40 (1000:1) high-voltage probe. Data were predominantly acquired *via* an NI USB-6356 data acquisition card and LabVIEW software. During experiments, the linear reciprocating motion of the OF-TENG was driven using an R-LP4 servo motor and monitored with an HZC-T-100KG tension sensor. Surface morphologies of PTFE and nylon films were analyzed using a Hitachi SU8020 cold field emission scanning electron microscope.

4.3. COMSOL Multiphysics simulation

The model encompasses four connection configurations for output electrodes with staggered alignment pairing of triboelectric materials, utilizing layered structures of PTFE, Nylon, and Fur as dielectric materials with relative dielectric constants of 2, 4, and 3, respectively, and an air domain dielectric constant of 1.0006. Both PTFE and Nylon have a thickness of 0.1 mm, with fixed charge densities of -250×10^{-6} μC m^{-2} on the PTFE surface and $+20 \times 10^{-6}$ μC m^{-2} on the Nylon surface. Electrodes on the reverse side of the triboelectric materials are designated as output terminals and reference ground potential terminals, respectively, with the series resistance between nodes neglected to streamline boundary conditions. The conductivity of both electrodes and the triboelectric conductive layer is set at 3.5×10^{-7} S m^{-1}. To enhance interface region simulation accuracy, ultra-fine triangular meshing with a maximum cell size of 0.01 mm is applied at the electrode–dielectric and dielectric–air interfaces, while the air domain employs a

standard triangular mesh with a maximum size of below 1 mm. The electrostatic behavior is governed by the following equations:

$$\vec{E} = -\vec{\nabla} \cdot V \quad (1)$$

$$\vec{\nabla} \cdot \left(\varepsilon_0 \varepsilon_r \vec{E}\right) = \rho \quad (2)$$

where $\vec{E}$ is the electric field, ε_0 is the relative permittivity of air, and ε_r is the relative permittivity of the materials.

Conflicts of interest

The authors declare no competing financial interest.

Data availability

All data supporting the findings of this study are included in the manuscript and the SI, or are available from the corresponding authors upon reasonable request.

Supplementary information is available. See DOI: **https://doi.org/10.1039/d5ee02523k**

Acknowledgements

The research was supported by the National Key R&D Project from the Minister of Science and Technology (2021YFA1201604 and 2021YFA1201601) and the Beijing Nova Program (20220484036 and 20240484565).

References

1 X. Li, J. Luo, K. Han, X. Shi, Z. Ren, Y. Xi, Y. Ying, J. Ping and Z. L. Wang, *Nat. Food*, 2022, **3**, 133–142.
2 Z. L. Wang, *Nature*, 2017, **542**, 160.
3 F. Chen, X. Dai, X. Wu, Z. Ding, Y. Gao, Y. Pang, T. Jiang, J. Luo, Z. Hong and Z. L. Wang, *Adv. Energy Mater.*, 2024, **32**, 2404891.
4 H. Ryu, H. J. Yoon and S. W. Kim, *Adv. Mater.*, 2019, **31**, e1802898.
5 P. J. Jeff Scruggs, *Science*, 2009, **323**, 1176–1178.
6 H. Joe, H. Roh, H. Cho and S.-C. Yu, *Energy*, 2017, **133**, 851–863.
7 C. Zhang, S. Yang, X. Dai, Y. Tu, Z. Du, X. Wu, Y. Huang, J. Fan, Z. Hong, T. Jiang and Z. L. Wang, *Nano Energy*, 2024, **128**, 109929.
8 T. Cheng, J. Shao and Z. L. Wang, *Nat. Rev. Methods Primers*, 2023, **3**, 38.
9 J. Zhang, M. L. Coote and S. Ciampi, *J. Am. Chem. Soc.*, 2021, **143**, 3019–3032.
10 H. Zou, Y. Zhang, L. Guo, P. Wang, X. He, G. Dai, H. Zheng, C. Chen, A. C. Wang, C. Xu and Z. L. Wang, *Nat. Commun.*, 2019, **10**, 1427.
11 Z. L. Wang and A. C. Wang, *Mater. Today*, 2019, **30**, 34–51.
12 Z. L. Wang, *Mater. Today*, 2017, **20**, 74–82.
13 Y. Zi, H. Guo, Z. Wen, M. H. Yeh, C. Hu and Z. L. Wang, *ACS Nano*, 2016, **10**, 4797–4805.
14 H. Yang, X. Liang, J. Kan, Z. L. Wang, T. Jiang and Z. Hong, *Nano Res.*, 2024, **17**, 7585–7592.
15 X. Dai, X. Wu, B. Yao, Z. Hong, T. Jiang and Z. L. Wang, *Adv. Funct. Mater.*, 2024, **34**, 2406288.
16 Z. Ding, E. Su, H. Yang, Z. Hong, Z. L. Wang and L. N. Y. Cao, *Device*, 2024, **3**, 100571.
17 L. Xu, T. Jiang, P. Lin, J. J. Shao, C. He, W. Zhong, X. Y. Chen and Z. L. Wang, *ACS Nano*, 2018, **12**, 1849–1858.
18 T. Jiang, H. Pang, J. An, P. Lu, Y. Feng, X. Liang, W. Zhong and Z. L. Wang, *Adv. Energy Mater.*, 2020, **10**, 2000064.
19 P. Lu, H. Pang, J. Ren, Y. Feng, J. An, X. Liang, T. Jiang and Z. L. Wang, *Adv. Mater. Technol.*, 2021, **6**, 2100496.
20 C. Shan, W. He, H. Wu, S. Fu, K. Li, A. Liu, Y. Du, J. Wang, Q. Mu, B. Liu, Y. Xi and C. Hu, *Adv. Funct. Mater.*, 2023, **33**, 2305768.
21 X. Li, L. Xu, P. Lin, X. Yang, H. Wang, H. Qin and Z. L. Wang, *Energy Environ. Sci.*, 2023, **16**, 3040–3052.
22 S. Yang, C. Zhang, Z. Du, Y. Tu, X. Dai, Y. Huang, J. Fan, Z. Hong, T. Jiang and Z. L. Wang, *Adv. Energy Mater.*, 2024, **14**, 2304184.
23 C. Zhang, L. He, L. Zhou, O. Yang, W. Yuan, X. Wei, Y. Liu, L. Lu, J. Wang and Z. L. Wang, *Joule*, 2021, **5**, 1613–1623.
24 I. Gonçalves, C. Rodrigues and J. Ventura, *Adv. Energy Mater.*, 2023, **14**, 2302627.
25 X. Li, D. Zhang, D. Zhang, Z. Li, H. Wu, Y. Zhou, B. Wang, H. Guo and Y. Peng, *Nanomaterials*, 2023, **13**, 1036.
26 Y. Chung, J.-M. Jeong, J.-H. Hwang, Y.-J. Kim, B.-J. Park, D. S. Cho, Y. Cho, S.-J. Suh, B.-O. Choi, H.-M. Park, H.-J. Yoon and S.-W. Kim, *Joule*, 2024, **8**, 2681–2695.
27 D. M. Lee, M. Kang, I. Hyun, B. J. Park, H. J. Kim, S. H. Nam, H. J. Yoon, H. Ryu, H. M. Park, B. O. Choi and S. W. Kim, *Nat. Commun.*, 2023, **14**, 7315.
28 A. Ahmed, Z. Saadatnia, I. Hassan, Y. Zi, Y. Xi, X. He, J. Zu and Z. L. Wang, *Adv. Energy Mater.*, 2017, **7**, 1601705.
29 B. D. Chen, W. Tang, C. He, C. R. Deng, L. J. Yang, L. P. Zhu, J. Chen, J. J. Shao, L. Liu and Z. L. Wang, *Mater. Today*, 2018, **21**, 88–97.
30 Y. Wang, X. Liu, Y. Wang, H. Wang, H. Wang, S. L. Zhang, T. Zhao, M. Xu and Z. L. Wang, *ACS Nano*, 2021, **15**, 15700–15709.
31 T. X. Xiao, X. Liang, T. Jiang, L. Xu, J. J. Shao, J. H. Nie, Y. Bai, W. Zhong and Z. L. Wang, *Adv. Funct. Mater.*, 2018, **28**, 1802634.
32 M. Yin, X. Lu, G. Qiao, Y. Xu, Y. Wang, T. Cheng and Z. L. Wang, *Adv. Energy Mater.*, 2020, **10**, 2000627.
33 W. Jiang, C. Chen, C. Wang, J. Li, M. Zhao, T. Xiang and P. Wang, *Energy Environ. Sci.*, 2023, **16**, 6003–6014.
34 Y. Ren, Z. Wang, J. Chen, F. Wu and H. Guo, *Energy Environ. Sci.*, 2024, **17**, 8829–8837.
35 Z. Li, C. Yang, Q. Zhang, G. Chen, J. Xu, Y. Peng and H. Guo, *Research*, 2023, **6**, 0237.
36 Y. Yu, Q. Gao, X. Zhang, D. Zhao, X. Xia, J. Wang, H. Li, Z. L. Wang and T. Cheng, *Energy Environ. Sci.*, 2023, **16**, 3932–3941.
37 T. Li, X. Wang, K. Wang, Y. Liu, C. Li, F. Zhao, Y. Yao and T. Cheng, *Adv. Energy Mater.*, 2024, **14**, 2400313.

38 Y. C. Pan, Z. Dai, H. Ma, J. Zheng, J. Leng, C. Xie, Y. Yuan, W. Yang, Y. Yalikun, X. Song, C. B. Han, C. Shang and Y. Yang, *Nat. Commun.*, 2024, **15**, 6133.
39 J. Zhang, Y. Yu, H. Li, M. Zhu, S. Zhang, C. Gu, L. Jiang, Z. L. Wang, J. Zhu and T. Cheng, *Appl. Energy*, 2023, **357**, 122512.
40 L. He, C. Zhang, B. Zhang, Y. Gao, W. Yuan, X. Li, L. Zhou, Z. Zhao, Z. L. Wang and J. Wang, *Nano Energy*, 2023, **108**, 108244.
41 F. Shen, Z. Li, H. Guo, Z. Yang, H. Wu, M. Wang, J. Luo, S. Xie, Y. Peng and H. Pu, *Adv. Electron. Mater.*, 2021, **7**, 2100277.
42 C. Zhang, L. Zhou, P. Cheng, D. Liu, C. Zhang, X. Li, S. Li, J. Wang and Z. L. Wang, *Adv. Energy Mater.*, 2021, **11**, 2003616.
43 B. Cao, P. Wang, P. Rui, X. Wei, Z. Wang, Y. Yang, X. Tu, C. Chen, Z. Wang, Z. Yang, T. Jiang, J. Cheng and Z. L. Wang, *Adv. Energy Mater.*, 2022, **12**, 2202627.
44 J. Han, Y. Liu, Y. Feng, T. Jiang and Z. L. Wang, *Adv. Energy Mater.*, 2022, **13**, 2203219.
45 W. Harmon, D. Bamgboje, H. Guo, T. Hu and Z. L. Wang, *Nano Energy*, 2020, **71**, 104642.
46 H. Sun, X. Xu, H. Kim, W. Jung, W. Zhou and Z. Shao, *Energy Environ. Mater.*, 2023, **6**, e12441.

